Supplemental Material

Lomb *et al.*

Crystal preparation

Monodisperse hen egg white lysozyme nanocrystals ($0.4 \times 0.4 \times 0.8$ μm^3) were prepared essentially as described previously [1]. To reduce the formation of larger crystalline assemblies, the crystallite slurry was incubated for 30 min at 15 ºC with 1.5 mg/ml proteinase K while gently shaking using a thermocycler (750 rpm) before crosslinking with glutaraldehyde [1]. Proteinase K was removed by pelleting the crystals by centrifugation and resuspension in 0.5 M Na-acetate pH 3.0. The crystals were resuspended in water for data collection. Sizing of the crystals was performed by transmission electron microscopy

Data collection.

The experiments were performed at LCLS at SLAC at the AMO (Atomic, Molecular and Optical Science) beamline [2] *in vacuo* (base pressure: 2×10^{-7} Torr, pressure jet injection conditions: 10^{-5} Torr) in the CFEL-ASG Multi-Purpose (CAMP) instrument [3], placed 2 m downstream of the nominal AMO instrument. A liquid micro-jet focused by a coaxial flow of helium to 4 μm diameter was operated at a flow rate of 12 -16 μl/min using a Shimadzu HPLC system to introduce the crystalline slurry into the CAMP instrument and to ensure rapid replenishment of the crystals to the interaction region. The crystallite concentration was adjusted such that the probability of a crystal being in the FEL-jet interaction region was ~70 %. That is, assuming a Poisson distribution of hits, and a crystal in the volume of $3 \times 3 \times 4$ μm^3 (3 μm FEL focus, 4 μm jet diameter), the crystal concentration was about $3 \cdot x\ 10^{10}$ per ml. A 2 μm in-line filter was used to eliminate larger crystal aggregates. The interaction of the X-rays and crystals takes place in the continuous liquid column, prior to the Rayleigh breakup of the jet into drops, so that X-ray scattering from the liquid is confined to a narrow vertical streak in reciprocal space. X-ray fluorescence from the water jet was filtered out by 2.9 μm parylene-N coated with 100 nm aluminum on each side in front of the pnCCDs. Diffraction data were recorded with a set of two movable X-ray pnCCD detector units [3] which were placed 66.0 mm and 68.6 mm downstream of the crystal-FEL interaction region, respectively. The detectors covered diffraction angles of 4.1º to 48º, thus recording high-angle diffraction to a resolution of 7.6 Å at the corner of the CCD. Each detector half consists of 512×1024 pixels of 75×75 μm^2. The detector system was synchronized with the FEL which was operating at repetition rate of 60 Hz.

For comparison with the virtual powder patterns calculated from the FEL data, conventional powder patterns of the same batch of lysozyme crystals were collected at room temperature at beamline 10SA at the Swiss Light Source in Villigen, Switzerland. To this end, wet crystallites were packed in 1 mm quartz capillaries. Data collection was performed using a PILATUS 6M detector [4], 10 keV X-rays (1.239 Å wavelength) focused to 30 x 50 μm^2 and attenuated to a flux of 4×10^{11} photons/s, and a capillary-to-detector distance of 1200 mm. The capillaries were exposed for 4-5 s while rotating 360º. The exposures were radially integrated with routines developed for the integration of SAXS data [5].

Data evaluation.

Bragg peaks were identified and located in all diffraction patterns of both detectors by applying a discrimination algorithm based on a local threshold. These thresholds were determined by calculating the average and its standard deviation over areas that are large compared to individual Bragg peaks but smaller than common distances of Bragg peaks on individual images. The threshold was set to 4 standard deviations above average value. In

order to identify a discriminated pixel as part of a Bragg peak at least three neighboring pixels are necessary that are above the local threshold as well. The center of each identified peak was chosen as the center of mass of every group of those identified pixels.
Local background subtraction was performed using a method similar to that implemented in DENZO [6]. Briefly, peaks identified by a peak searching algorithm were surrounded by three circles. All intensity inside the inner circle was considered to consist of peak intensity + background intensity, whereas all intensity between the outer and middle circles was considered to be background intensity only. The median value of the local background intensity thus found was then subtracted from pixel intensities in the area inside the inner circle to yield the Bragg peak's intensity.
After correction of peak positions with respect to pulse-to-pulse wavelength variations in every individual diffraction pattern, virtual powder patterns were generated by summing up all Bragg peaks observed in all diffraction patterns of the 70 fs, 78 fs, 85 fs, 100 fs, 150 fs , 200 fs, 250 fs, 300fs, and 400 fs pulse durations into virtual powder patterns, respectively.
Since the rotational motion of the nanocrystals during their interaction with the extremely short X-ray pulses is negligible, a correction for the speed with which a reflection moves through the Ewald sphere (Lorenz correction) is not strictly applicable. However, the probability of observing a reflection can be derived as follows. Given a random orientation of the reciprocal lattice, the shape of a three-dimensional diffraction peak (hkl) in reciprocal space can be approximated with a sphere of radius r. The probability of this sphere intersecting the Ewald sphere depends on the solid angle under which it is seen from the origin of reciprocal space. For a general reflection (hkl) this solid angle can be obtained from the angle $\angle\alpha = \arctan\frac{r}{\left|\vec{S}\right|}$ of the cone circumscribing the sphere in reciprocal space and which has its apex at (000) (see Figure S1) as follows

$$2\pi(1-\cos\alpha) = 2\pi\left(1-\cos\left(\arctan\left(\frac{r}{\left|\vec{S}\right|}\right)\right)\right) = 2\pi\left(1-\frac{1}{\sqrt{1+\left(\frac{r^2}{\left|\vec{S}\right|^2}\right)}}\right)$$

Normalization by the probability of observing (000), which is unity, and expressing $\left|\vec{S}\right|$ in terms of the wavelength and the scattering angle 2ϑ , the probability of observing a reflection (hkl) becomes: $p(obs,hkl) = 1-\frac{1}{\sqrt{1+\frac{r^2\lambda^2}{4\sin^2\vartheta}}}$

This function shows a rapid falloff with increasing scattering angle. A estimate of *r* is difficult to make, but as this is a continuous function of 2ϑ, to a first approximation this effect affects the data like an increased conventional Wilson B-factor and was therefore neglected for most calculations in the current study. However, for small *r*, it can be shown that this function has the same shape as the canonical Lorentz factor $\frac{1}{\sin^2\vartheta\cos\vartheta}$ for powder diffraction data [7], so for the determination of the Wilson B and k values, the calculation of

R-factors and correlation coefficients and for molecular replacement, the normal Lorentz correction mentioned above was applied.

Figure S1: Ewald construction to derive the resolution dependence of the hit probability

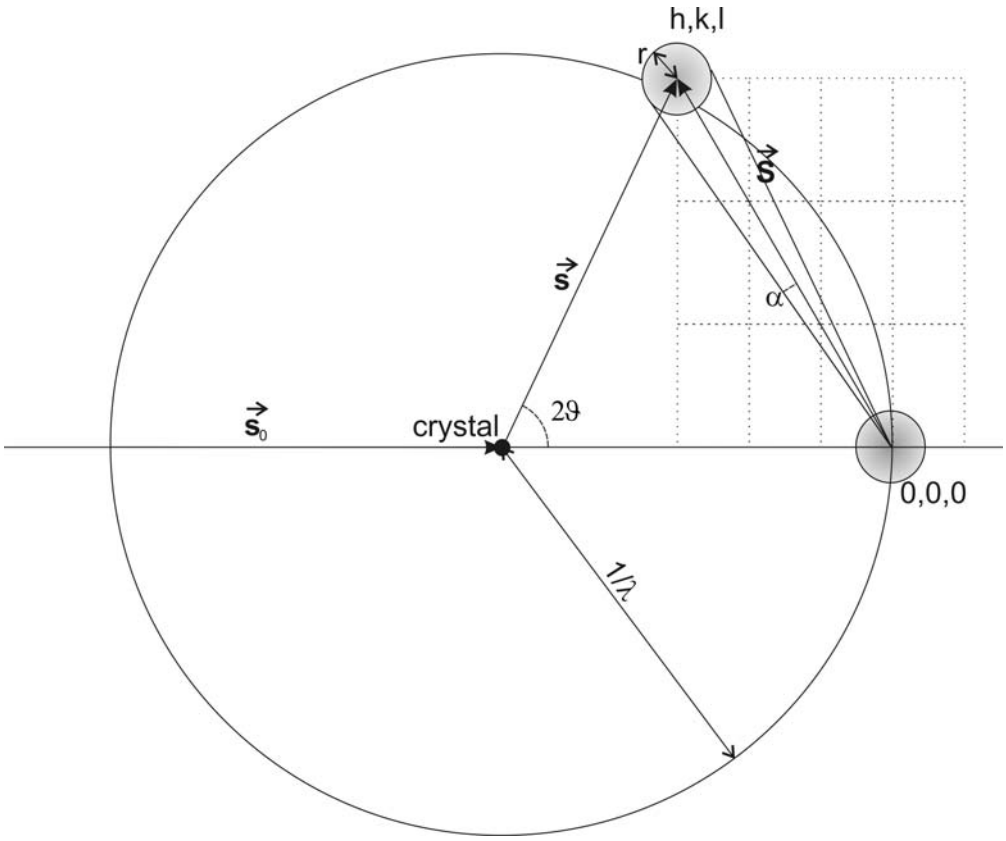

Generation of virtual powder patterns enabled refinement of the detector geometry (the x and y positions with respect to the direct beam and its orientation) from the shape and position of the Debye-Scherrer rings. Circularity of the powder rings was characterized by a maximum correlation in tangential direction. The z positions (translation along the direct beam) of both detectors were determined by optimizing the ring radii for the known lattice parameters of lysozyme. Using this information, the virtual powder patterns were corrected and radially integrated excluding areas with strong scattering from the water jet. The resulting one-dimensional intensity profiles were modeled by a sum of pseudo-Voigt functions

$$I(2\vartheta) = \sum_{hkl} A_{hkl} \cdot \left\{ \sum_{hkl} \left[GL \cdot \left(\frac{e^{-\left(\frac{2\vartheta - 2\vartheta_{hkl}}{2\gamma}\right)^2}}{\sqrt{2\pi\gamma^2}} \right) \right] + \left[(1-GL) \cdot \left(\frac{\gamma}{\pi\left(\gamma^2 + (2\vartheta - 2\vartheta_{hkl})^2\right)} \right) \right] \right\}$$

centered at the $2\vartheta_{hkl}$ values (scattering angles) expected for the reflections (hkl) for a given combination of wavelength and unit cell parameters. In this expression, GL is a number between 1 (pure Gaussian) and 0 (pure Lorentzian) which determines the relative Gaussian/Lorentzian character and determines the width of the peak. By fitting the parameters of this function, the detector distance and the unit cell parameters to the observed data, each peak was assigned the appropriate index hkl and the peak area A_{hkl} was extracted.

Because

$$\int_{-\infty}^{\infty}\left\{\left[GL\cdot\left(\frac{e^{-\left(\frac{2\vartheta-2\vartheta_{hkl}}{2\gamma}\right)^2}}{\sqrt{2\pi\gamma^2}}\right)\right]+\left[(1-GL)\cdot\left(\frac{\gamma}{\pi\left(\gamma^2+\left(2\vartheta-2\vartheta_{hkl}\right)^2\right)}\right)\right]\right\}d2\vartheta=1$$

these A_{hkl} are related to the intensities I_{hkl} as follows:

$I_{hkl}\propto\frac{A_{hkl}}{m_{hkl}\cdot p(obs,hkl)}$ where m_{hkl} is the multiplicity of the reflection (hkl) and $p(obs,hkl)$ is the probability of observing (hkl).

The determined intensities were corrected for the effects of beam polarization using the expression in [8] adapted to the experimental geometry:

$P=1-2p\left[1-\left(\sin\varphi\cdot\sin 2\vartheta\right)^2\right]+p\left\{1+\left(\cos 2\vartheta\right)^2\right\}$ where φ is the polar angle on the detector at which the reflection is observed, starting from the plane of polarization, and 2ϑ is the scattering angle. The polarization *p* is the probability of finding the polarization plane of a photon in the horizontal plane, and was taken to be 0.99.

Molecular replacement solution:

Polarization-, Lorentz- and multiplicity-corrected intensities were imported into CCP4 file format and converted to structure factor amplitudes using SFTOOLS (CCP4). A search model was constructed from protein data bank entry 1vds (**DOI:**10.2210/pdb1vds/pdb) by removing water molecules and manually rotating and translating the molecule such that its long axis lies along the crystallographic *a* axis and its center of mass lies in the origin to have an orientation and position that is entirely unrelated to the correct one. The resulting reoriented model was used for molecular replacement using FSEARCH [9] using the SFX datasets without taking packing into account, *i.e.* using exclusively the structure factor amplitudes. In each case, the best solution in terms of R-factor corresponded to the correct solution after reduction to the same asymmetric unit and/or removal of a space group-allowed origin shift (see Figure S2).

Figure S2: Molecular replacement solution
XZ-slice through the 6-dimensional search space colored by R-factor of the molecular replacement calculation as determined by FSEARCH [9] using the structure factor amplitudes extracted from the 78 fs data. A sharp minimum is found, illustrating the quality of the solution.

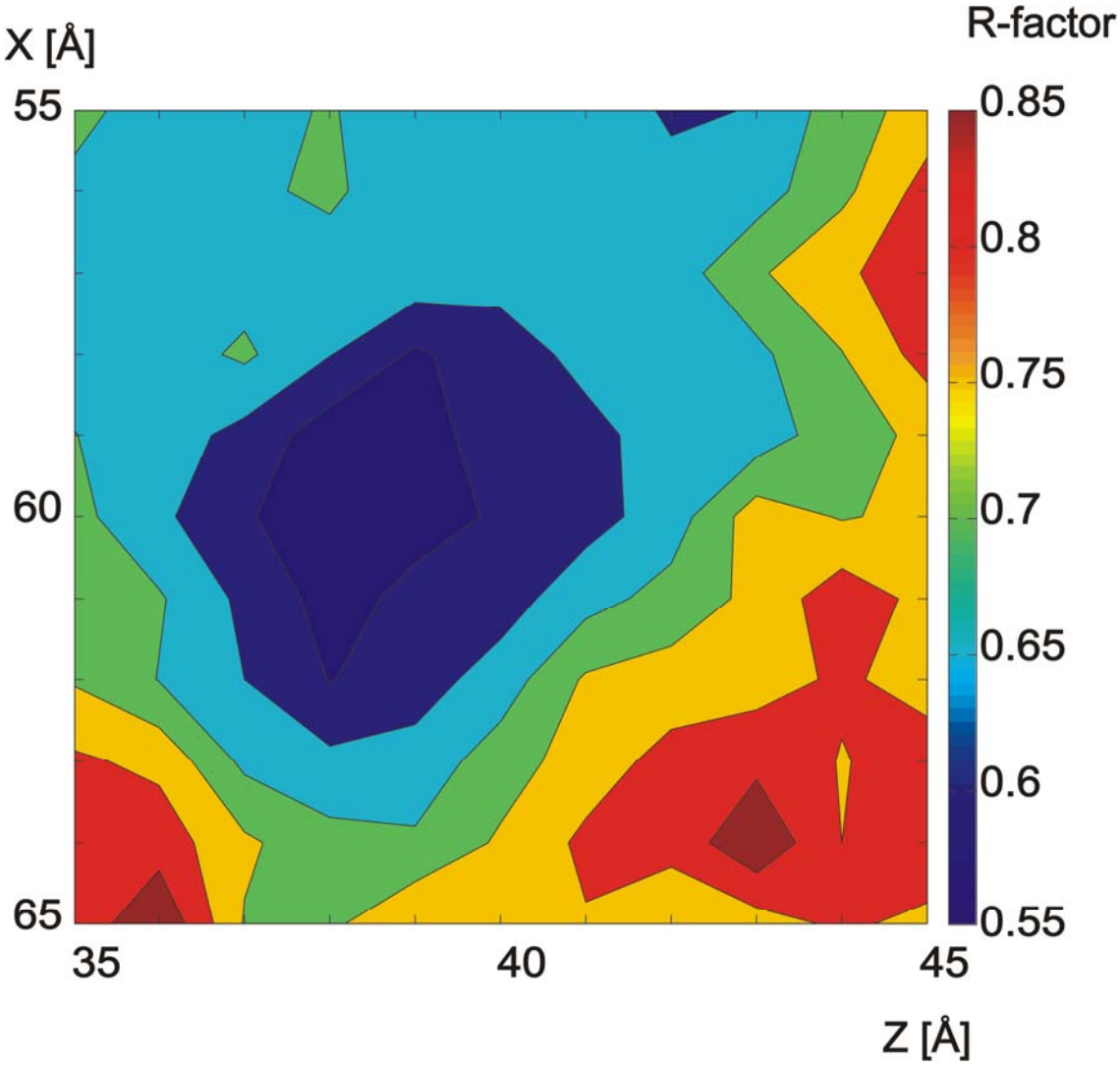

Internal consistency of the SFX data

For each pulse duration, the set of images was randomly divided into two equally sized parts, which were converted into 1-dimensional intensity profiles that were compared (Figure S3: red and blue lines). The data do not show significant differences.

Figure S3. Internal consistency of the SFX data

For each pulse duration, the set of images was randomly divided into two equally sized parts, which were converted into 1-dimensional intensity profiles that could be compared (red and blue lines). Data are shown exemplarily for 70 fs(A), 150 fs (B) and 400 fs (C).

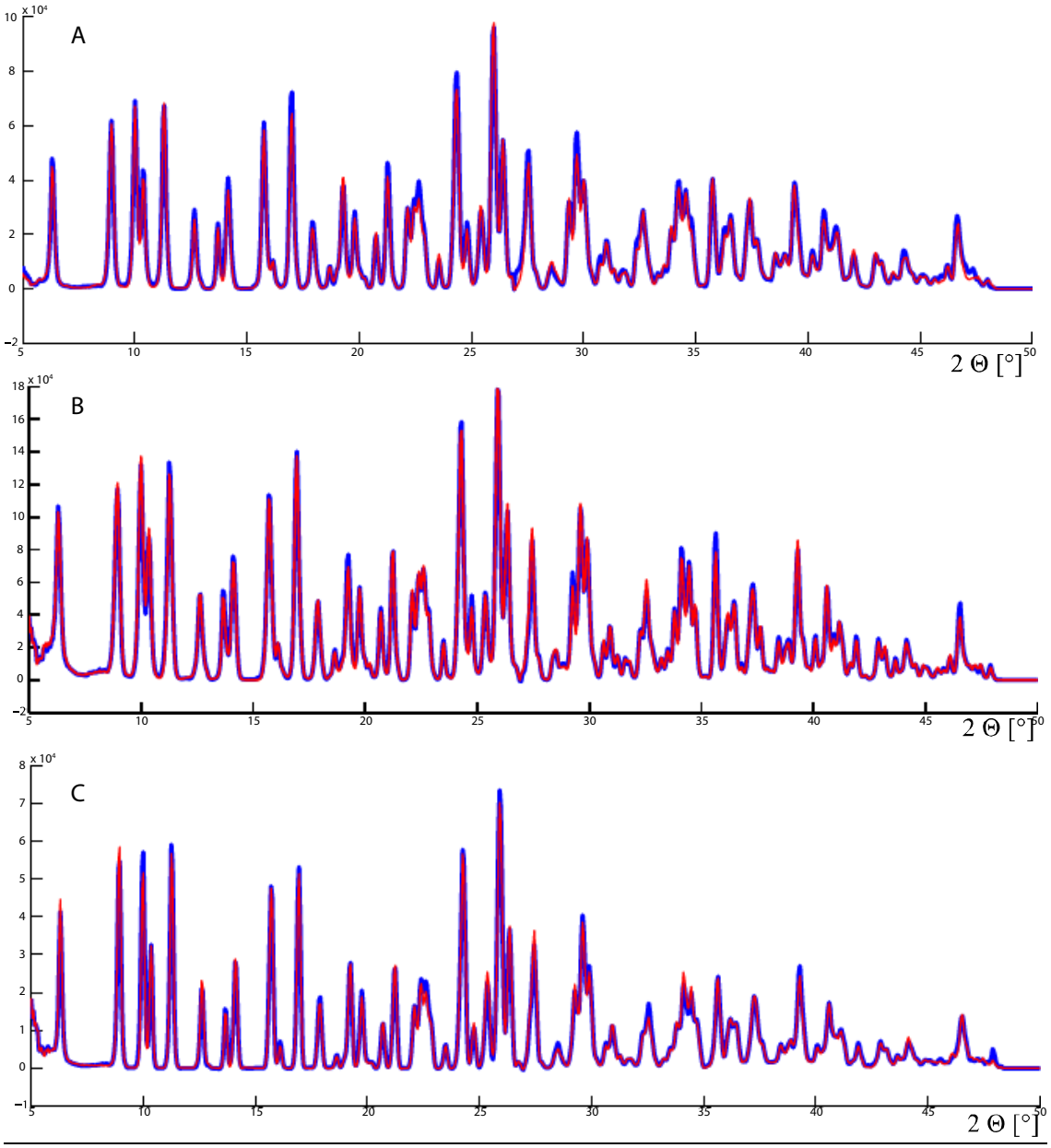

Classification of diffraction patterns according to intensity

Diffraction patterns were classified for each pulse duration according to the scattered intensity integrated over all Bragg peaks into 20 groups containing the same number of diffraction patterns. Powder patterns were generated for each individual group. These groups were then pooled into 5 classes with similar powder pattern intensities plus one class containing mainly empty diffraction patterns which was neglected in the analysis.

Analysis of detector saturation effects

Gain settings on the pnCCD detector were set such that the electron capacity of each pixel was slightly below the maximum of the analog-to-digital converter. If the number of electrons created exceeds the capacity of a pixel electrons spill into neighboring pixels without any loss in the integrated signal. It is important to realize that spilling into neighboring pixels affects the data by broadening the calculated powder rings.

Figure S4: Radiation damage for diffraction patterns of similar scattered intensities
A subset of the diffraction patterns of each pulse lengths showing intensities like the most intense 400 fs diffraction pattern was used for the analysis. Data were treated identical to Figure 2D of the main text.

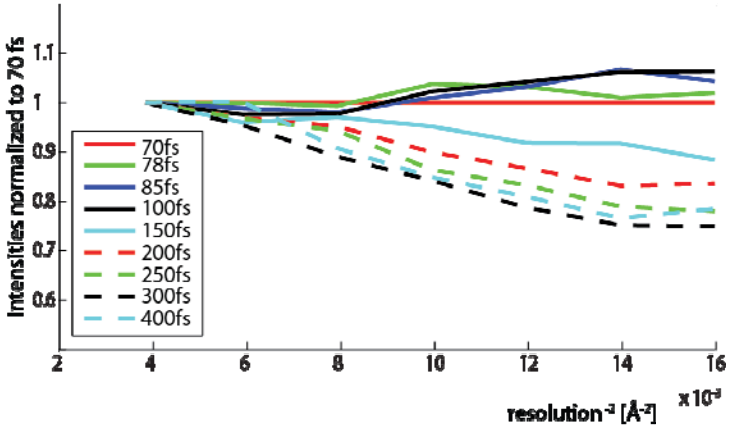

Figure S5: Schematic representation of the resolution dependent decrease of scattered intensity during an FEL pulse.
The high resolution contribution (red box) disappears early on during the pulse in contrast to the low resolution part (blue box). See also Figure 4 in [10].
The average ionization per atom at the end of a 100 fs pulse is 1.5 for a crystal in the middle of the X-ray beam. With an Auger decay-time of ~10 fs for carbon, the ionization causes both a fast electronic rearrangement that results in a general reduction of Bragg intensities similar to the effect of a Debye-Waller factor and a (slower) displacement of the generated ions during the pulse, resulting in the formation of a plasma. The ensuing disorder will manifest itself first at short length scales and, as the electron temperature rises and the molecular fragments move, progress towards longer distances, finally destroying the crystalline order altogether [11] and ultimately resulting in an explosion of the sample. The final measured signal is the sum of all intensities during the X-ray pulse.

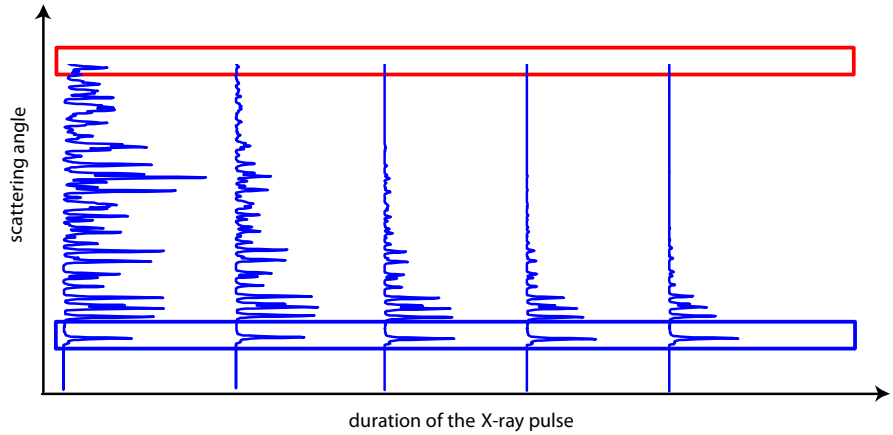

Figure S6A. R-factors between the various SFX datasets. In general, the R-factor increases as the difference in pulse length between two data sets increases.

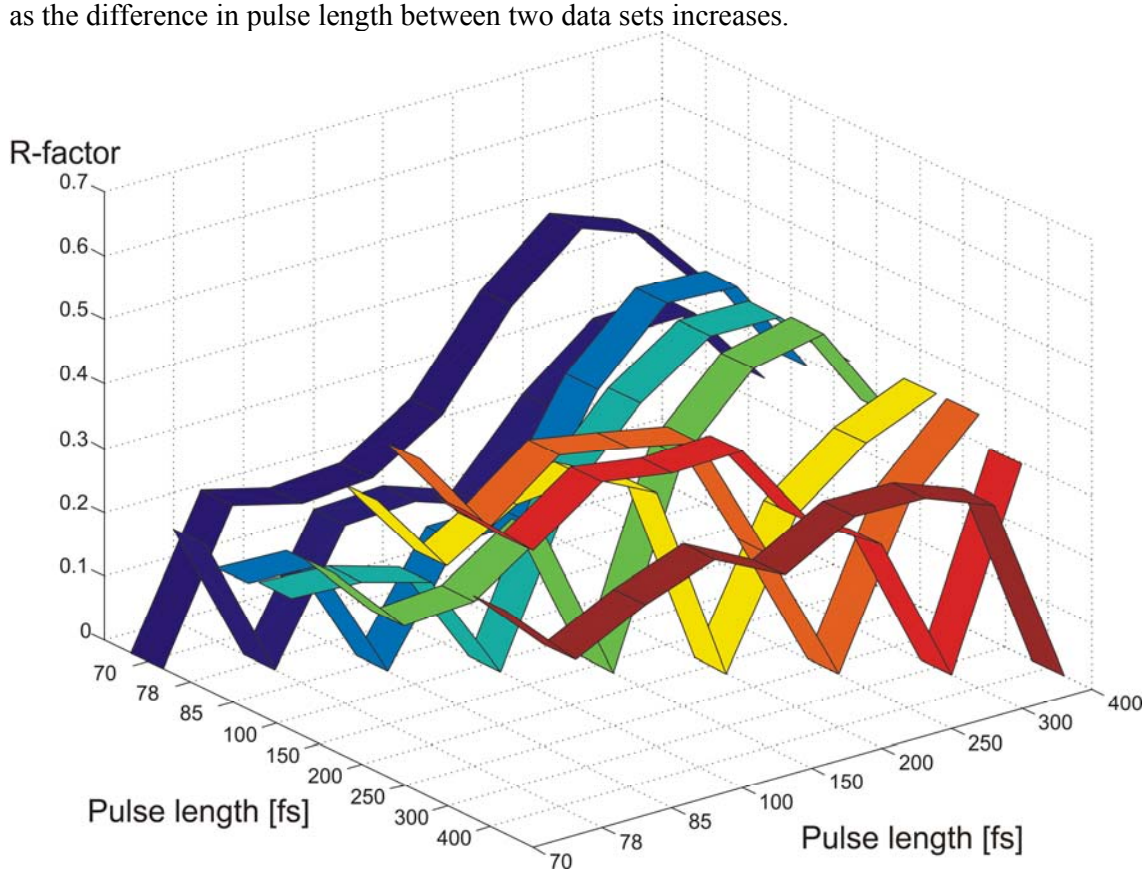

Figure S6B. Bin-wise R-factors of the SFX data (collected at different pulse lengths) vs. data collected at a 3rd generation synchrotron (SLS 1, SLS2)
At high resolution, the pixel size of the detector no longer allows the separation of reflections according to scattering angle, leading to a sharp increase in R-factor. Nevertheless, within experimental error, both a higher R-factor between SFX and synchrotron data seems apparent and an increase of the R-factor with resolution.

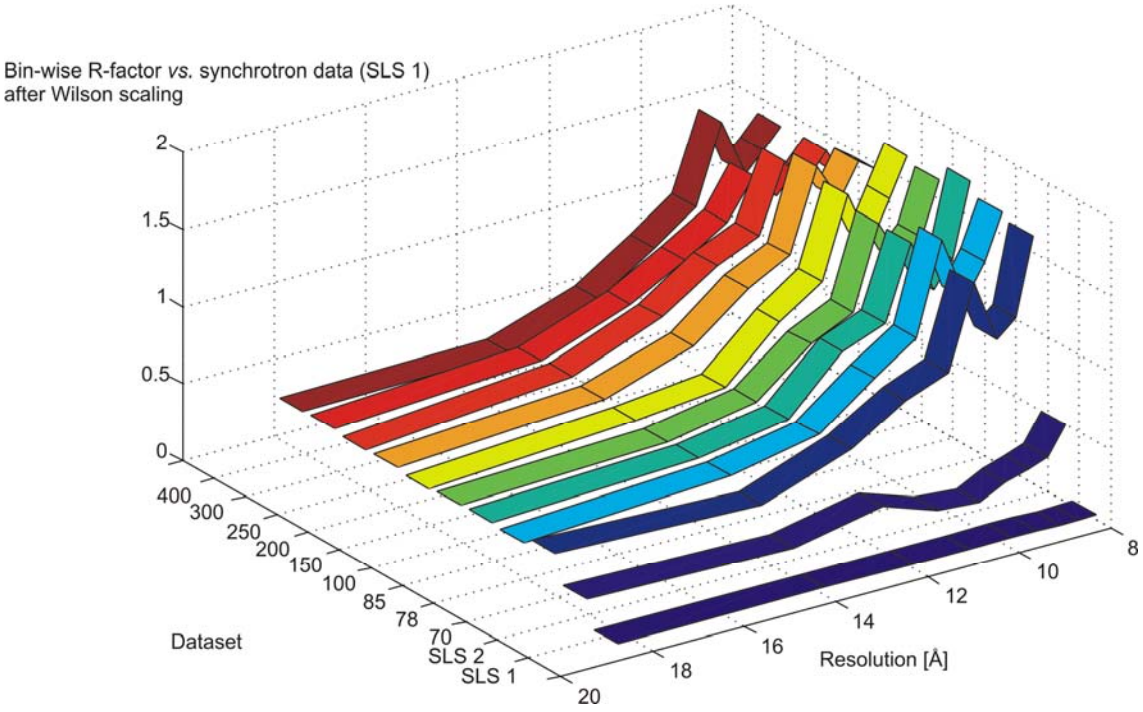

Figure S7. Intensity of integrated Bragg peaks as a function of pulse length
Within experimental errors, the intensities of some reflections do not vary with pulse lengths; others change smoothly but not monotonically with pulse lengths. See also Figure 4 in [10].

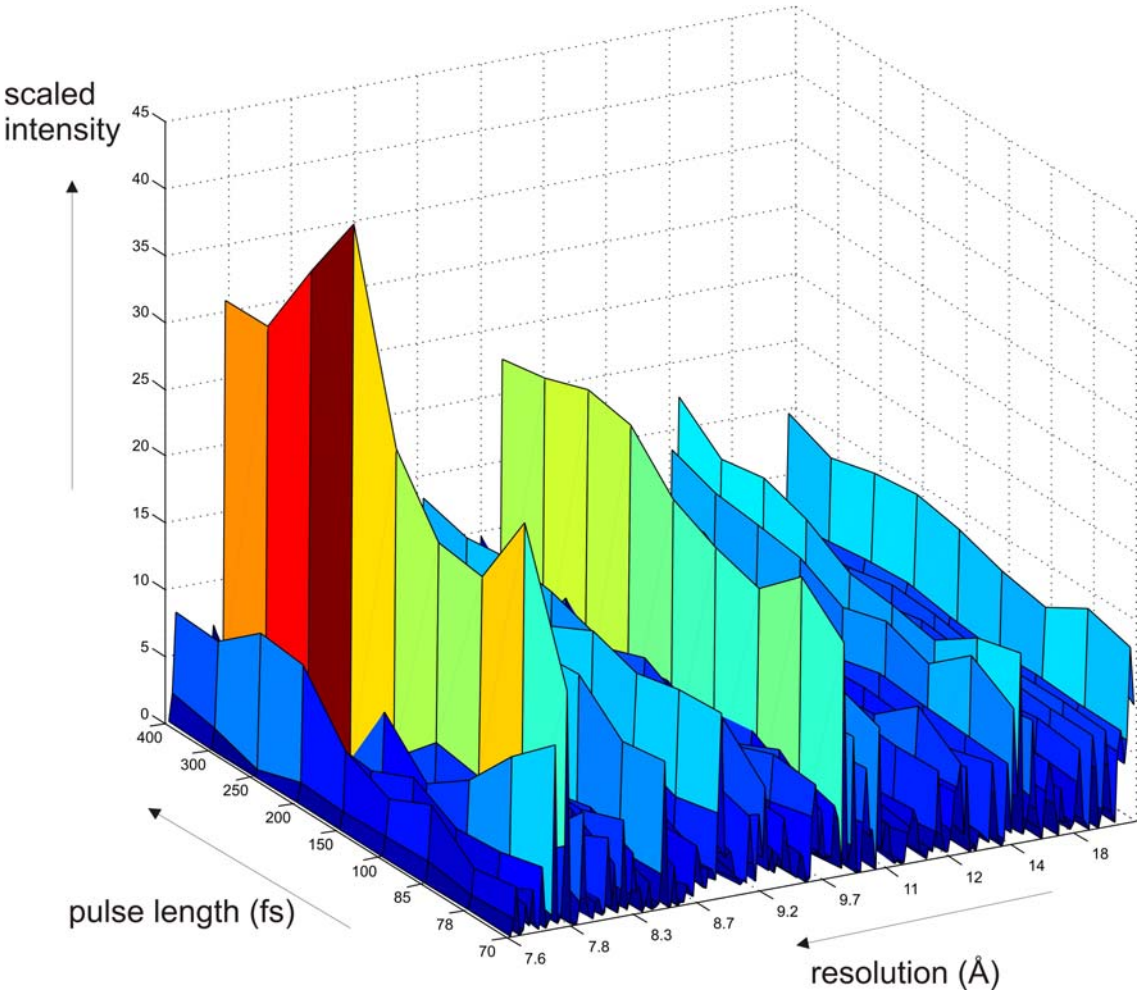

Figure S8 Effects of random displacements in a crystal lattice
A. Fourier transform of a regularly spaced one-dimensional lattice *l* of 800 unit cells. **B**. Fourier transform of the same lattice, after random displacements have been added to the position of each lattice point. A rapid falloff of the Bragg maxima with resolution *q* is accompanied by a marked increase in diffuse scattering with increasing *q*.

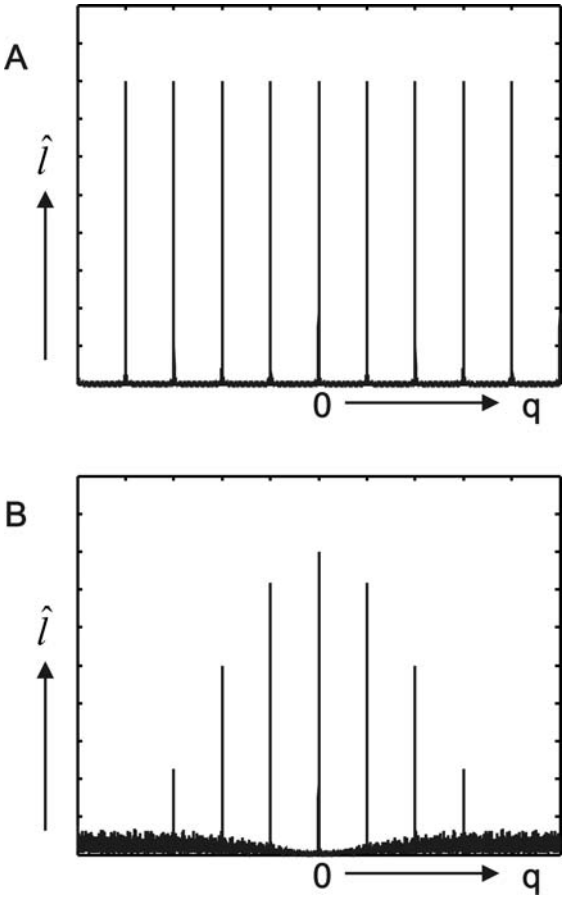

Using a Debye-Waller factor to correct for a time dependent displacement of the atoms during the FEL pulse:
Assuming that the average displacement σ of an atom changes linearly with time *t* by a factor *a* during an FEL pulse the intensity for a single reflection, integrated over time, can be calculated as follows:

$$\sigma(t) \approx at$$

$$I(t) = I_0 e^{-4\pi^2\sigma^2(t)q^2} = I_0 e^{-4\pi^2 a^2 t^2 q^2}$$

$$\int I(t)dt = \int I_0 e^{-4\pi^2 a^2 t^2 q^2} dt = \frac{erf(2\pi atq) I_0}{4\sqrt{\pi} aq}$$

In order to use the Debye-Waller factor to correct for the integrated intensities their natural logarithm should show a q^2-dependence. Approximation by a Taylor expansion around q=0, where T is the time at the end of the pulse, leads to:

$$\ln\left(\int_0^T I(t)dt\right) = \ln\left(\frac{erf(2\pi aTq)I_0}{4\sqrt{\pi}aq}\right) \approx \ln(T\cdot I_0) - \frac{1}{3}\cdot 4\pi^2 a^2 T^2 q^2 + \frac{8}{45}\cdot 4\pi^4 a^4 T^4 q^4 + \ldots$$

$$\ln\left(\int_0^T I(t)dt\right) \approx \ln(T\cdot I_0) - \frac{1}{3}\cdot 4\pi^2 \sigma(T)^2 q^2 + \ldots$$

So to a first approximation, the q^2 dependence hold true and the effective B-factor is about a third of what would be the B-factor calculated from the atomic displacements at the end of the pulse (at time T).

To ensure higher terms in the Taylor expansion do not influence the Wilson plot appreciably the q^2 term has to be larger than the q^4 term:

$$\frac{1}{3}\cdot 4\pi^2 a^2 T^2 q^2 >> \frac{8}{45}\cdot 4\pi^4 a^4 T^4 q^4$$

$$\rightarrow \sigma(T) << \frac{0.44}{q}$$

Since q never exceeds 0.02 Å^{-1}, the plot should be approximately linear up to atomic displacements of several Å.

Reference List

[1] J. C. Falkner, M. Ali, J. Jamison, J. Zhang, S. Adrianse, R.Simpson, M. Calabretta, W. Radding, G.Phillips Jr, and V. Colvin, Chemistry of materials. **17**, 2679 (2005).

[2] J. D. Bozek, The European Physical Journal Special Topics **169**, 129 (2009).

[3] L. Strüder, S. Epp, D. Rolles, R. Hartmann, R. Holl, G. Lutz, H. Soltau, R. Eckhart, C. Reich, *et al,* Nuclear Instruments and Methods in Physics Research A **614**, 483 (2010).

[4] C. Broennimann, E. F. Eikenberry, B. Henrich, R. Horisberger, G. Huelsen, E. Pohl, B. Schmitt, C. Schulze-Briese, M. Suzuki, T. Tomizaki, *et al*., J. Synchrotron. Radiat. **13**, 120 (2006).

[5] A. Menzel Matlab macros for the integration of cSAXS data. 2010. http://www.psi.ch/sls/csaxs/software/cSAXS

[6] Otwinowski, Z, W. Minor, in *Methods in Enzymology,* Jr. C.W.Carter, R.M.Sweet, Eds. (Academic Press, 1997), pp. 307-326.

[7] A. Guinier, X-ray diffraction *In Crystals, Imperfect Crystals, and Amorphous Bodies* (Cover Publications, Inc, 1994).

[8] W. Kabsch, Journal of Appl. Cryst. **21**, 916 (1988).

[9] Q. Liu, A. J. Weaver, T. Xiang, D. J. Thiel, Q. Hao, Acta Crystallogr. D Biol. Crystallogr. **D59**, 1016 (2003).

[10] C. Caleman, G. Huldt, F. Maia, C. Ortiz, F. Parak, J. Hajdu, D. van der Spoel, H. Chapman, and N. Timneanu, ACS Nano. **5**, 139 (2011).

[11] A. Barty, accepted by Nature Photonics.